PAPER • OPEN ACCESS

A solid–liquid hybrid electrolyte for lithium ion batteries enabled by a single-body polymer/indium tin oxide architecture

View the article online for updates and enhancements.

A solid–liquid hybrid electrolyte for lithium ion batteries enabled by a single-body polymer/indium tin oxide architecture

Taehoon Kim[1,2] **, Dae-Yong Son**[1]**, Luis K Ono**[1] **, Yan Jiang**[1,3] **and Yabing Qi**[1,*]

[1] Energy Materials and Surface Sciences Unit (EMSSU), Okinawa Institute of Science and Technology Graduate University (OIST), 1919-1 Tancha, Onna-son, Okinawa 904-0495, Japan
[2] Department of Safety Engineering, Incheon National University (INU), 119 Academy-ro, Yeonsu-gu, Incheon 22012, Republic of Korea
[3] Energy Materials and Optoelectronics Unit, Songshan Lake Materials Laboratory, Dongguan, Guangdong 523808, People's Republic of China

E-mail: Yabing.Qi@OIST.jp

CrossMark

Abstract
Solid-state electrolytes have received much attention because of their high safety and cycling stability for lithium ion batteries. However, the interfacial contact issue of solid electrolytes with the electrode and active material hinders their practical use. Herein, for the first time, we demonstrate a hybrid electrolyte that combines a solid polyethylene terephthalate (PET) electrolyte with an organic liquid electrolyte to provide synergetic benefits over a single electrolyte. The single-body PET electrolyte/In_2O_3–SnO_2 (ITO; 110 nm, 150 nm, 260 nm and 340 nm) electrode was prepared by vacuum sputtering deposition. The simplicity of the electrode composite (e.g., conductive additive-free, solvent-free and binder-free) and its gapless structure between the polymer substrate and the active material significantly impede the formation of by-products from the decomposed electrolyte as well as the growth of an unstable solid electrolyte interphase upon cycling. In addition, the cell configuration of the Li metal/organic electrolyte/PET/ITO electrode enables a process called 'Li$^+$ caging', which leaves some of the lithium ions in the PET due to the different ion transfer kinetics of the heteroionic interfaces. The hybrid electrolyte cell not only shows an excellent rate capability at 100–400 mA g^{-1}, but also exhibits high cycling stability (>1200 cycles). Our study lays a cornerstone for the development of practical hybrid electrolytes for lithium ion batteries with improved stability.

Supplementary material for this article is available online

(Some figures may appear in colour only in the online journal)

---

* Author to whom any correspondence should be addressed.

1. Introduction

Recent developments in lithium ion batteries have led to numerous studies focusing on improving their charge capacity, power density, rate capability and cycle life. Whereas the electrochemical performance of batteries continues to improve, stability and safety issues still remain [1–5]. The liquid electrolytes employed in commercial lithium ion batteries possess high ionic conductivities, which is beneficial for rapid interface kinetics. Problems arise when an undesired redox reaction takes place between the constituents of the electrode and liquid electrolyte chemicals upon charge–discharge. During the initial electrochemical cycle, the battery electrolyte undergoes redox reactions with the electrodes to form a passivation layer, namely a solid electrolyte interphase (SEI) layer. The SEI hinders electron transfer from/to the electrolyte but allows lithium ions to migrate [6, 7]. The SEI layer is of great importance for establishing kinetic stability, particularly to a larger open circuit voltage [6]. However, the formation of an unstable SEI layer accompanying non-uniform lithium ion deposition and dendrite growth can result in critical internal short circuits and severe battery failure [1, 8–11]. Further growth of the non-uniform SEI layer not only causes a loss of electrical conductivity between the active material particles but also isolates lithium ions from the host electrode, thereby making it permanently unavailable (i.e. 'dead Li^+') [3, 12–14]. Decomposition of liquid electrolyte by redox reaction can also trigger a series of degradation processes such as solvent co-intercalation, release of gaseous products with crack formation, modification of pristine active materials, volume expansion of electrodes, contact losses between conductive additive, current collector and binder, dissolution of SEI into the electrolyte and lithium ion plating [12, 15, 16]. In particular, lithium ion plating, dendrite growth and the formation of 'dead Li^+' are the major obstacles to the practical use of next-generation lithium ion batteries. Several attempts have been made to solve these degradation issues with liquid electrolytes, such as surface fluorination by LiF coating, stabilizing active material particles by graphene or polymer coatings [poly(3,4-ethylenedioxythiophene)-co-poly(ethylene glycol) or poly(3,4-ethylenedioxythiophene) polystyrene sulfonate], creating an artificial SEI layer (lithium phosphorus oxynitride, lithium alkyl carbonate, LiF deposition), tuning ion transportation and tailoring the electrolyte with additives [17–28]. However, application of special treatments often requires additional steps during the fabrication process, which can increase the manufacturing cost of devices. In addition, incorporation of an extra component as a treatment carries potential risks that can adversely affect the (electro)chemical system. Also, the high flammability of organic electrolytes in many commercialized lithium ion batteries poses critical safety concerns. Therefore, solid-state electrolytes have received considerable attention recently as they could counter the aforementioned stability and safety issues. They benefit from high thermal stability, non-flammability, a longer cycle life, mechanical robustness and simplicity of design [29–31]. Furthermore, these electrolytes are known to be effective in suppressing dendrite growth during charge and discharge [19, 32]. However, several challenges remain in the practical use of solid-state electrolytes. They have an interfacial contact issue with the active material and electrode, resulting in high interfacial impedance [31, 33, 34]. The low conductivity of lithium ions at room temperature is another major problem, especially for solid polymer electrolytes [35–37]. Although ionic conductivity in an inorganic solid electrolyte is rather high, the presence of grain boundaries can pose considerable resistance [37–39]. These aforementioned problems of solid-state electrolytes often result in lower electrochemical performance and stability. Therefore researchers have shown a growing interest in developing hybrid electrolytes to take advantages of both electrolytes. Previous research reported a hybrid polymer/oxide/ionic liquid solid electrolyte with composition of PEO_{20}–$NaClO_4$–$5\%SiO_2$–$x\%$ 1-ethyl-3-methylimidazolium bis(fluorosulfonyl)imide (where $x = 50, 70$) for sodium metal batteries exhibiting a gravimetric capacity of 62.7 mA h g^{-1} for 100 cycles [40]. A recent study employed a solid–liquid hybrid electrolyte that combines a $Li_{1.3}Al_{0.3}Ti_{1.7}(PO_4)_3$ inorganic solid electrolyte with an organic liquid electrolyte [i.e. lithium hexafluorophosphate ($LiPF_6$) in ethylcarbonate (EC), ethyl methylcarbonate, diethylcarbonate (DC) and fluoroethylene carbonate]. The cell with the hybrid electrolyte had a gravimetric capacity of 146.6 mA h g^{-1} for 50 cycles [41]. Another study has demonstrated a hybrid solid electrolyte prepared by blending $Li_7La_3Zr_2O_{12}$ particles with an liquid electrolyte. With a $Li/LiCoO_2$ configuration, the cell gravimetric capacity is 110–140 mA h g^{-1} for 150 cycles [42]. Ion transfer kinetics at the interface between the solid and liquid electrolytes is the key factor for developing a working hybrid electrolyte cell [43, 44].

In this study, we demonstrate a hybrid electrolyte that combines a solid-state electrolyte, made from polyethylene terephthalate (PET), with an organic liquid electrolyte. Indium tin oxide (In_2O_3–SnO_2; ITO) was deposited on the PET film as an active material for the battery anode. An ITO coating on a PET substrate is a widely used and commercially proven combination employed in a number of different applications such as electroluminescent lighting, touchscreens and flexible solar cells [45–47]. The strong and uniform adhesion between PET and ITO enables the motive force for ion migration in the hybrid electrolyte. The PET film consists of the same plastic material that can be obtained from any PET bottle, and can be easily recycled. Due to the PET substrate, the electrode possesses good flexibility and mechanical properties [48, 49]. The tensile strength and Young's modulus of PET are 50 MPa and ∼2000 MPa, respectively. These excellent mechanical properties of PET can be compared with other polymeric electrolyte materials. For instance, a garnet ($Li_7La_3Zr_2O_{12}$)-based hybrid solid electrolyte with poly(vinylidene fluoride-co-hexafluoropropylene) polymer exhibits a tensile strength of only 6.9 MPa and a Young's modulus of 12.5 MPa for the polymer membrane, although it is still considered to be a durable electrolyte material [50]. PET has also been proven to be an effective material for battery separators [48, 51–53].

PET not only maintains good electronic insulation, but also provides a high electrolyte affinity [49, 53]. Furthermore, this polymer possesses a superior thermal stability and is inexpensive. The commercially available PET material for packing has high thermal stability at different temperatures (e.g. -18 °C to 200 °C) [54] . The degradation of PET by heat begins at near to the melting point of the polymer (260 °C). On the other hand, some of the widely known polymer materials for solid electrolytes are prone to degradation at high temperatures. For example, polyethylene oxide (PEO) has a melting temperature of 68 °C and a lower thermal stability than PET. A previous study by Sun *et al* employed PET plastic as an anode material for lithium ion batteries [55]. The charge compensation mechanism of PET can be explained by the redox reaction between the intercalated lithium ions and the polyester polymer, $(C_{10}H_8O_4)_n$, in PET, where two lithium ions can be stored providing a reversible gravimetric capacity of 150 mA h g^{-1} [55]. The configuration of the Li metal/organic electrolyte/PET/In_2O_3–SnO_2 electrode enables 'Li$^+$ caging' in PET substrates, forming a diffusion pathway for lithium ions. Previous studies have demonstrated polymer electrolytes with embedded lithium ions [56, 57]. As for the current study, the caging of lithium ions in the PET layer stemming from the heteroionic interfaces between the electrolytes would result in a coulombic efficiency slightly higher than 100%. The amount of liquid electrolyte [lithium hexafluorophosphate in EC, DC and dimethylcarbonate (DMC)] added to the hybrid electrolyte cell could be reduced by 20% in volume compared with a liquid organic electrolyte cell. We also entirely eliminate the standard components (i.e. polymer binder, conductive additive and mixing solvent) commonly used in preparing electrodes for lithium ion batteries in order to reduce the interphase resistance as well as improve compatibility between the electrode and the electrolytes. The specific capacity for a PITO 150 (Li metal/liquid electrolyte/150 nm ITO-PET electrolyte) cell was approximately 110 mA h g^{-1} for 100 cycles at 100 mA g^{-1}, with a similar gravimetric capacity level for more than 1200 cycles. Also, the hybrid electrolyte cell had an excellent rate capability at a charge density of 100–400 mA g^{-1}.

2. Experimental

2.1. PET ITO (PET-ITO: PITO) electrode preparation

The PET electrolyte/ITO electrodes (denoted as PITOs) were prepared by a vacuum sputter deposition method using an ULVAC (Japan) CAM-S vacuum sputtering system inside a Class 1000 (ISO 6) clean room. ITO was sputtered on the commercially purchased PET films with different thicknesses using a physical vapour deposition process. A vapour stream composed of the sputtering material diffuses in the vacuum chamber hitting the PET, and is thus deposited on it. Chemically inert Ar gas was introduced into the vacuum chamber as a controlled gas during the deposition process to maintain the pressure at less than 1.0×10^{-4} Pa. The pressure increased to

0.1 Pa during the sputtering operation. The deposition method is of the deposition-up type, and the sputter cathode is a 2-inch magnetron cathode with a target diameter of 50.8 mm. PET film was placed on a rotation stage with a rotation speed of 7.0 rpm, and the distance between the PET substrate and the ITO target (source) was 150 mm. The Ar flow rate was set to 10.0 sccm, and the sputtering power for ITO was 110 W. The operation was conducted at room temperature for 2000, 2625 and 4550 s in order to produce 110 nm (PITO 110 nm), 150 nm (PITO 150 nm) and 260 nm (PITO 260 nm) ITO, respectively, on the PET surface.

2.2. Cell assembly and electrochemical characterization

Cell assembly was done in an Ar glove box ($H_2O < 1.0$ ppm, $O_2 < 1.0$ ppm). The synthesized PITOs were cut into working electrode pieces with a diameter of 16 mm. CR2032 coin cells were prepared by assembling Li metal (counter electrode), PITO, springs and stainless steel spacers using a hydraulic crimping machine (MTI, MSK-110). A solution of 1 M LiPF$_6$ in EC, DC and DMC was employed as the electrolyte with a volume ratio of EC:DC:DMC = 1:1:1. PITO in a pristine state was labelled as PITO REF with no current applied. The galvanostatic tests were carried out using an eight-channel battery tester (NEWARE, Battery Test Station). The electrochemical cells were discharged and charged in the voltage range between 0.05 V and 2.0 V with a current density of 100 mA g^{-1} for 100 cycles. For the rate capability test, current densities of 100, 200, 300 and 400 mA g^{-1} were applied for 11 cycles each. The current density and capacity were calculated based on the weight of the single body unit that combines the PET film and ITO active material (e.g. a 0.95 mA current was applied to a 9.51 mg PET-ITO body to introduce 100 mA g^{-1}). The electrochemical impedance spectroscopy (EIS; Autolab PGSTAT204 with a FRA32 module) analyses were conducted for pristine cells (PITO REF), cells cycled for the rate capability test (PITO RT), cells cycled 100 times (PITO $\times$ 100) and cells cycled 500 times (PITO $\times$ 500). The frequency range was 0.1 Hz to 100 kHz with an AC amplitude of 5 mV. The EIS curves were fitted using the ZVIEW2 application.

### 2.3. Material characterization

The electrochemically cycled coin cells were disassembled inside the Ar glove box. The extracted electrodes were firstly cleaned using DMC solution. Then they were dried overnight as in previous material characterizations. Secondary-ion mass spectrometry (SIMS) was utilized to visualize the depth-wise elemental distribution, elemental mapping and general depth profiling. SIMS visualization was carried out based on the positive ion detection mode (PID) of the SIMS spectrometer (Kratos Axis ULTRA), which was equipped with a quadrupole mass spectrometer (HAL 7, Hiden Analytical) and an ion sputter gun (IG20, Hiden Analytical). The mass spectrometer collected the *m/q* signals from 1.0 to 170.0 amu for the SIMS

visualization. The introduced beam for the SIMS measurement/sputtering was a 1 keV Ar^+ primary beam with a current of 50 nA and diameter of 100 μm. The angle of the beam to the sample surface was 45°. The initial pressure of the SIMS chamber was 10^{-9} mbar, while it was 10^{-6} mbar during operation. The surface chemistry of the pristine and cycled PITO was examined by x-ray photoelectron spectroscopy (XPS; AXIS Ultra HSA KRATOS) with an Al Kα = 1486.6 eV x-ray source. The operation was performed under an ultra-high vacuum (10^{-9} Torr) at 15 kV (applied power 150 W). The XPS binding energy (eV) was calibrated by measuring the Fermi edge (E_F = 0 eV) on an Au surface. The energy resolution was evaluated to be 0.14 eV and the applied sample bias voltage was −9.0 V. As for XPS data analyses, the background was treated with a Shirley-type function and data fitting was performed with a Gaussian–Lorentzian function using the CasaXPS application. To calibrate the spectral shift, 284.9 eV (C 1s) was used. The surface morphologies of PET and ITO were compared under different cycled conditions using a scanning electron microscope (SEM; FEI Quanta 250 FEG). X-ray diffraction (XRD) spectra were collected by a Bruker D8 x-ray diffractometer (x-ray source Cu Kα radiation = 8 keV) in the range of 2θ = 10°–80° with a step scanning increase of 0.02°. A JEOL ARM 200 F scanning tunnelling electron microscope (STEM) was employed to obtain STEM images at different cycled states, as well as conduct energy-dispersive x-ray spectroscopy (EDX). The STEM was operated with the acceleration voltage of 200 kV, and the pressure in the specimen chamber was 10^{-5} Pa. The resolution at 200 kV was estimated to be 0.078 nm. Sn L, In L, O K, C K and P K edges were used to map the PITO under the different cycling conditions. For observation of the ITO particles, a JEOL JEM-1230R TEM was employed with an acceleration voltage of 100 kV. The TEM resolution was 0.2 nm (100 kV).

3. Results and discussion

The single body PITO electrode employed in the current work was prepared by a vacuum sputter deposition method. ITO was sputtered on PET substrates at thicknesses of 110, 150, 260 and 340 nm, which correspond to film resistivities of 100.4, 85.1, 52.6 and 20.8 Ω sq^{-1}, respectively (see figure S1 in the supplementary information available online at stacks.iop.org/JPD/54/475501/mmedia). In contrast to the conventional battery electrodes, no binder and no conductive additive were used, and thus no solvent was used to prepare the electrode (figure 1(a)). The calendaring process with a twin roller was also omitted, and there was no heat treatment, which had the benefit of lowering the fabrication cost. The design of the PITO is illustrated in figure 1(a). A lithium ion battery with a PITO electrode is likely to be dendrite-free after cycling, owing to the simplicity of the material composition and the embedded design (see figure S2 in the supplementary information). ITO not only functions as a transparent electrical conductor but also serves as a battery active material,

as evidenced in the galvanostatic profile (figure 1(c)) The electrochemical process can be described by the following reactions [58–60]:

$$SnO_2 + 2Li + 2e^- \rightarrow SnO + Li_2O \tag{1}$$

$$SnO + 2Li + 2e^- \rightarrow Sn + Li_2O. \tag{2}$$
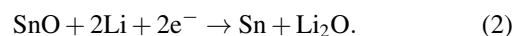
Combining equations (1) and (2) leads to the expressions

$$Sn + xLi + xe^- \rightarrow Li_xSn \, (0 \leqslant x \leqslant 4.4) \tag{3}$$

$$SnO_2 + 4Li + 4e^- \rightarrow Sn + 2Li_2O. \tag{4}$$
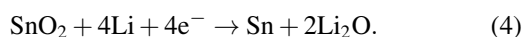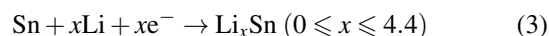
Also, the charge compensation process for In_2O_3 is written as follows:

$$In_2O_3 + 6Li + 6e^- \rightarrow 2In + 3Li_2O \tag{5}$$

$$In + xLi + xe^- \rightarrow Li_xIn \, (0 \leqslant x \leqslant 4.4). \tag{6}$$
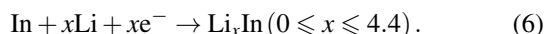
Equation (4) explains the irreversible conversion reaction during the initial electrochemical cycle which is responsible for the large capacity loss with the reduction of SnO_2 into metallic Sn, forming a Li_2O matrix. On the other hand, equation (3) indicates the reversible alloying/dealloying reactions between Sn and lithium ions, providing charge capacities on further cycles. However, this reaction is also associated with the large volume change of Sn (∼200%), which in turn results in pulverization of the electrode with continuous capacity fading and internal strain (or stress) [61–63]. The conversion reaction and the (de)alloying reaction are usually observed in tin oxide-based electrodes. Indium also appears to be capable of providing some charge capacity, showing a similar reaction to tin oxide [64]. One of the key features of the PITO cell is the 'Li$^+$ caging' process during charging and discharging (figure 1(a)). The employment of PET as a solid electrolyte and separator for the PITO enables the caging of lithium ions inside PET, possibly by changing their linearity in the polymer chain and crystallinity during cycling. This will be discussed in detail later. To understand the electrochemical properties of the electrode, PITO cells were prepared with the different thicknesses of ITO film (PITO 110 nm, PITO 150 nm, PITO 260 nm and PITO 340 nm). The PITO cells were cycled in the voltage range between 0.05 and 2.0 V with an applied current of 100 mA g^{-1}. The cycle performance of the PITO cells with different ITO film thicknesses is compared in figure 1(b). The PITO 150 nm cell was chosen for further electrochemical and material characterizations as it revealed an excellent rate capability. In most cases, the initial discharge capacity continued to increase with the increment of ITO thickness due to the larger amount of active material. The number of lithium ions introduced during the initial stage affects the number of lithium ions caged inside the PET
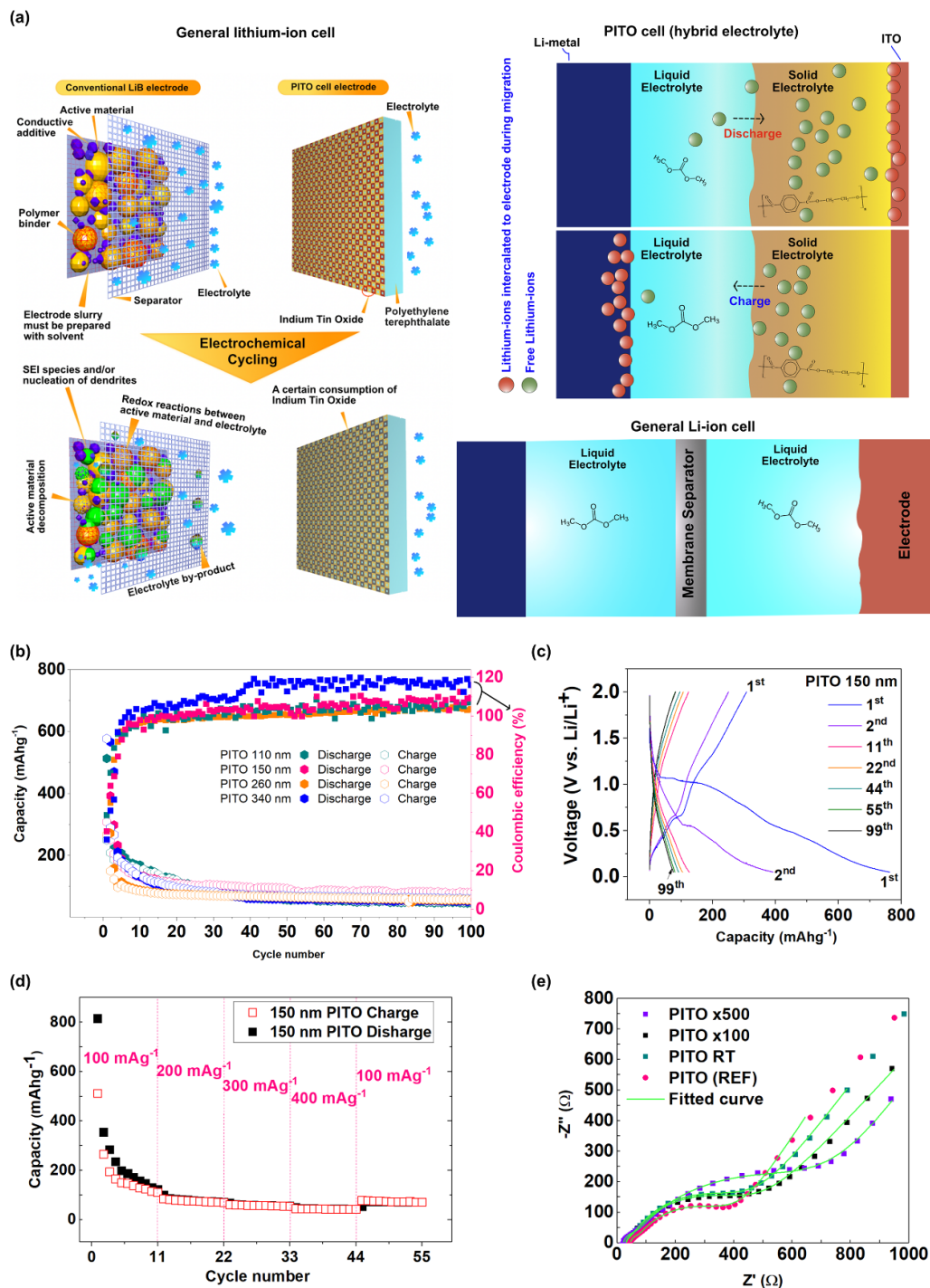
Figure 1. (a) Schematic drawing showing the conventional lithium ion battery electrode and newly developed PITO. (b) Coulombic efficiency and cycling performance of PET/ITO cells with ITO thicknesses of 110 nm (PITO 110 nm), 150 nm (PITO 150 nm) and 260 nm (PITO 260 nm) under a current rate of 100 mA g^{-1}. (c) Galvanostatic profile of a PITO 150 nm cell at a current rate of 100 mA g^{-1} for 100 cycles. (d) Rate capability test with charge rates of 100, 200, 300 and 400 mA g^{-1}. (e) Nyquist plot of the results of electrochemical impedance spectroscopy (EIS) for a pristine cell (PITO REF), a cell cycled under rate capability test conditions (PITO RT), a cell cycled 100 times (PITO × 100) and a cell cycled 500 times (PITO × 500). Green curves indicate EIS fittings.

substrate. This is why the PITO 340 nm sample had a higher coulombic efficiency of ∼120%. The coulombic efficiency became slightly higher than 100% for all cells (PITO 110 nm ∼108%, PITO 150 nm ∼110%, PITO 260 nm ∼105%, PITO 340 nm ∼120%). The coulombic efficiency will be even higher

at the same ITO thickness (e.g. PITO 110 nm ∼128%) if more lithium ions are stored in PET by adjusting the open-circuit voltage to a different range, i.e. 0.1–1.9 V (figure S3 in the supplementary information). An efficiency higher than 100% signifies that the number of lithium ions deintercalated from the

J. Phys. D: Appl. Phys. **54** (2021) 475501

T Kim *et al*

PITO upon charging is higher than the number of lithium ions intercalated into the electrode upon discharging. This observation is likely to be attributed to the different ion transfer kinetics of the heteroionic interfaces between the liquid electrolyte and the solid electrolyte on charge–discharge [43, 44]. The different ion transfer kinetics can be assigned to the discrepancy in the migration process, as well as in the activation energy barriers between charge and discharge [43, 44]. A long-term cycling test (over 1250 cycles) was also conducted, and the key electrochemical properties compared with other studies that employed Sn, SnO_2, ITO cells with an organic electrolyte (see figure S15 in the supplementary information). There was a dramatic loss of capacity during the initial cycle (figures 1(b) and (c)). This capacity loss is irreversible, and is a common feature for any SnO/SnO_2-based electrode. In particular, without any conductive additives and polymer binders, this capacity decrease will be steeper during the initial stage. At this stage, lithium ions are taken from the counter electrode (Li metal) and intercalated into the PITO electrode upon discharging, but a smaller number of lithium ions are deintercalated from the electrode after charging, causing a low coulombic efficiency. As mentioned earlier, this result can be explained mainly by the irreversible reduction of SnO_2 into metallic Sn, forming a Li_2O matrix, and pulverization of the electrode on cycling. On the other hand, in further cycles the PITO cell reveals a coulombic efficiency greater than 100% due to the different ion transfer kinetics between the solid electrolyte and the liquid electrolyte. As illustrated in figure 1(a), migration of lithium ions would be fast in the liquid electrolyte, whereas the migration becomes less smooth in the PET layer. On discharge, the PET cell can reach the target potential in a relatively short time as the ITO electrode layer is very thin (110–340 nm). At this moment, the rest of the introduced lithium ions are caged into the solid electrolyte. On charging, lithium ions deintercalate from the PITO electrode. Similarly, lithium ions are caged in the PET layer, but the number the caged ions would be less than in the discharged state. On subsequent cycles, the battery capacity becomes stable. This could be also confirmed by the long-term cycling results, which showed a coulombic efficiency of ∼110% on average for 1278 cycles (figure S15 in the supplementary information). For the rate capability test (PITO RT), currents of 100, 200, 300 and 400 mA g^{-1} were applied (figure 1(d)). There was little change in the achieved gravimetric capacity even at a higher charge rate (400 mA g^{-1}), which was four times higher than the initial rate, indicating good consistency at the electrode interphase. This observation implies the formation of a stable and non-growing SEI against the dynamic rate changes, due to the absence of conductive additives, polymer binders and residual solvents, and the gapless structure between the PET substrate and the active ITO material.

Figure 1(e) compares the EIS measurements in the pristine state (PITO REF), after the rate capability test (PITO RT) with 55 cycles, after 100 cycles (PITO × 100) and after 500 cycles (PITO × 500) with fittings (green plots). The refinement parameters and equivalent circuit are presented in the supplementary information (table S1). The resistances associated with the electrolyte (R_{el}), the SEI layer (R_{SEI}) and charge transfer (R_{CT})

were compared under the different cycling conditions. The first semicircle in the high-frequency range (∼10^5 Hz) can be attributed to the SEI layer (R_{SEI}). The large semicircle in the medium-frequency range (∼10^3 Hz) is likely to be ascribed to the charge transfer resistance (R_{CT}). At the interphase, the impedance behaviour can be modelled by a parallel combination between a resistance (R_{CT} or R_{SEI}) and a double-layer capacitance. Constant phase elements (CPE1 and CPE2) appear to be more suitable for the modelling. In contrast to the conventional battery electrodes, the spectrum in the medium-frequency range closely resembles a quarter circle rather than a semicircle. This observation can be explained by the formation of a small R_{SEI} with a very large R_{CT} spectrum that combines a notable contribution from the semi-infinite diffusion process in the low-frequency range, which leads to a distinct Warburg impedance. The R_{el} values for PITO REF, PITO RT, PITO × 100 and PITO × 500 were evaluated to be 44.8, 30.65, 28.31 and 20.0 Ω, respectively, whereas R_{CT} was 328.7 Ω for PITO REF, 376.9 Ω for PITO RT, 386.6 Ω for PITO × 100 and 663.3 Ω for PITO × 500. R_{SEI} of PITO RT, PITO × 100 and PITO × 500 were 9.01, 11.8 and 24.86 Ω, respectively. The values of electrolyte resistance (R_{el}) are somewhat higher than those of the conventional SnO/SnO_2-based electrodes [65–67]. The embedded structure of ITO behind PET can give rise to R_{el} as it shields the large contact area between the electrode and the electrolyte, yet allows lithium ions to diffuse into PET/ITO through the electrolyte. There is a continuous decrease of R_{el} with increasing electrochemical cycles, especially with higher cycle numbers. A lithium ion diffusion channel inside PET seems to be established. On the other side, the diffusion coefficients (D_{Li}) were evaluated to be 2.879×10^{-8}, 5.542×10^{-8}, 7.457×10^{-8} and 8.497×10^{-8} cm^2 s^{-1} for PITO REF, PITO RT, PITO × 100 and PITO × 500, respectively. These values are comparable to the previously reported lithium ion diffusion coefficients in graphitic anodes (∼10^{-7} to ∼10^{-11} cm^2 s^{-1}) [68, 69]. It is of interest to note that the lithium ion diffusion coefficient of PITO cells also rose notably upon cycling. Another important trend is the impedance change of R_{SEI}, which is ascribed to SEI formation. The PITO RT cell was cycled 55 times with current rates of 100, 200, 300 and 400 mAg^{-1}, showing a R_{SEI} of 9.01 Ω. This value is significantly lower than for conventional electrodes as well as some electrodes/cells specially developed for mitigating unstable SEI formation (see table S2 in the supplementary information) [70–76]. Surprisingly, the increment of SEI resistance (R_{SEI}) upon severe cycling (PITO × 100 and PITO × 500) is likely to be slight. This result might be explained by the gapless structure between the active material (ITO) and the PET substrate with the absence of conductive additives and polymer binders, which prevents further growth of the SEI. A schematic drawing of the lithium ion caging process is shown in figure 2(a). Upon discharging, lithium ions intercalate into the thin ITO film, but some of them tend to stay inside the PET substrate close to the ITO side. In contrast, lithium ions deintercalate from the electrode upon charging, migrating back to the counter electrode (Li metal). Similarly, there are some residual lithium ions staying inside the PET, but close to the electrolyte side. The caged lithium ions inside PET
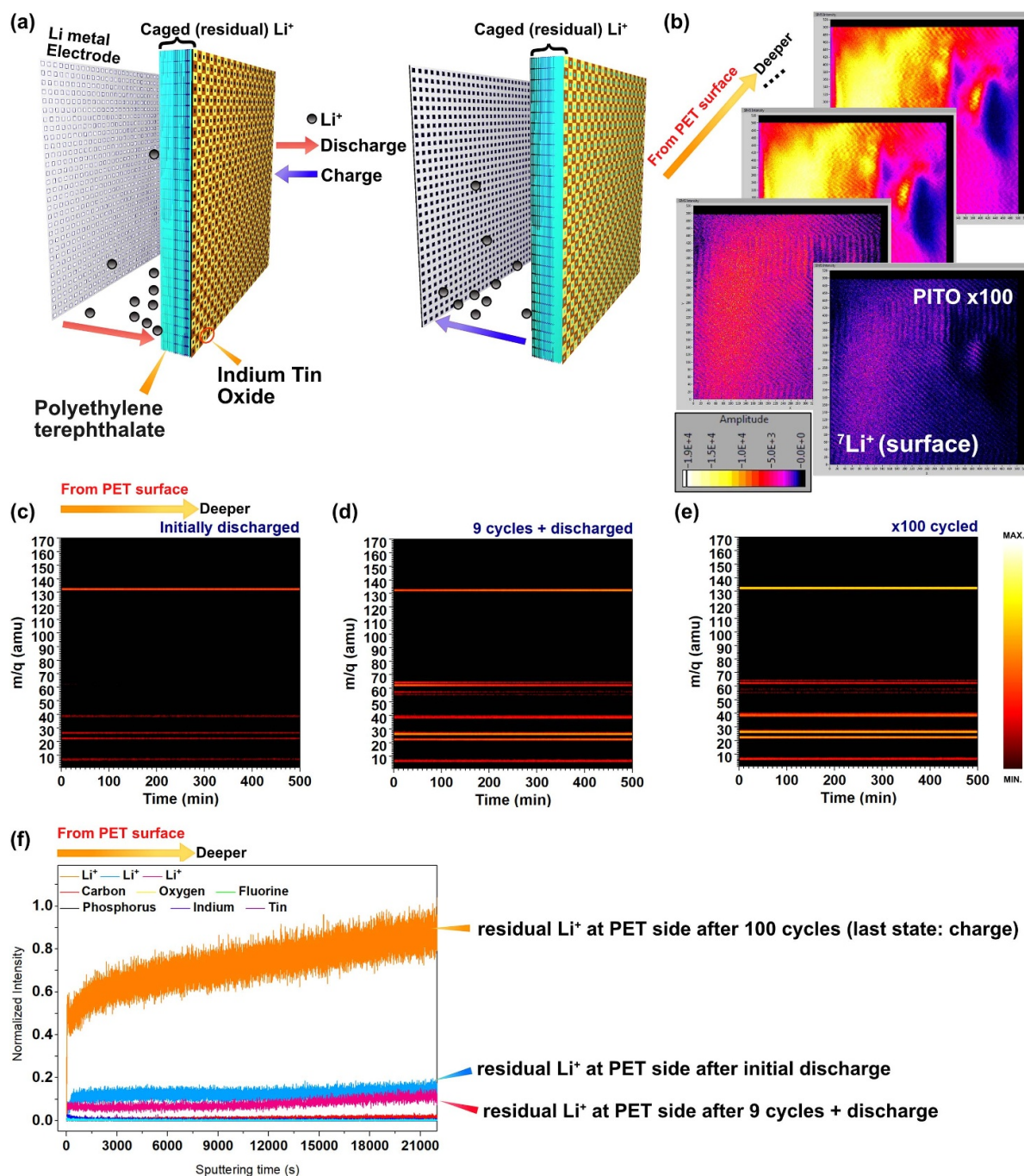
Figure 2. (a) Illustration of the lithium ion caging process in PET on charge and discharge. (b) $^7Li^+$ surface mapping at different depths. (c) Visualized elemental depth profile based on the positive-ion detection (PID) measurements from 1.0 to 170.0 amu of an initially discharged PITO 150 nm electrode, (d) a 9.5-cycled PITO 150 nm electrode and (e) a 100-cycled PITO 150 nm electrode. (f) Normalized SIMS depth profile of Li, C, O, F, P, In and Sn for initially charged, 9.5-cycled and 100-cycled PITO 150 nm electrodes.

after 100 cycles (last state, charged) were visualized by surface mapping with different depths (figure 2(b)). SIMS in PID mode was conducted by collecting the mass spectra between 1.0 and 170.0 amu so as to understand the compositional properties under different cycling conditions. We visualized the elemental depth profile based on the PID measurements, as can be seen in figures 2(c)−(e). This approach provides the particular benefit of depicting the elemental distribution (figures S6–S8 in the supplementary information). After the initial

discharge to 0.05 eV, four notable bands could be observed at around 7.0, 22.0, 27.0 and 133.0 amu, respectively. These bands correspond to the fragments of Li^+ (6.0 and 7.0 amu), $LiCH_3^+$ (22.0 amu), $C_2H_3^+$ (27.0 amu), $C_2H_4^+$ (28.0 amu), $C_8H_4O_2^+$ (132.0 amu) and $C_8H_5O_2^+$ (133.0 amu). $LiCH_3^+$ is likely to be the key fragment involved in the migration of lithium ions. The other carbon-based fragments are the typical molecules normally reported in PET material [77]. After 9.5 cycles (last state, discharged), additional bands could be

identified at around 56.0, 58.0, 63.0 and 65.0 amu (figure 2(d)). The bands at 58.0 and 65.0 amu can be assigned to the fragments of $C_2H_2O_2^+$ (58.0 amu) and $C_5H_5^+$ (65.0 amu). The intensity of the $C_2H_4^+$ (28.0 amu) fragment increased. The presence of $C_2H_4^+$ (28.0 amu), $C_2H_2O_2^+$ (58.0 amu) and $C_5H_5^+$ (65.0 amu) indicates the increment of linear structures in PET after the electrochemical cycles [77]. Also, there were some decomposed products from the redox reactions between the electrolyte and PET, as evidenced by the formation of weak bands at approximately 56.0 and 63.0 amu. After 100 cycles (last state, charged), the intensity of Li^+ (6.0 and 7.0 amu), $LiCH_3^+$ (22.0 amu), $C_2H_3^+$ (27.0 amu) and $C_8H_5O_2^+$ (133.0 amu) fragments became stronger, as shown in figure 2(e). The relocation of the caged lithium ions towards the PET surface upon charging tends to contribute to the notable rise in the intensity of the Li^+ (6.0 and 7.0 amu) and $LiCH_3^+$ (22.0 amu) bands. On the other hand, the intensity of $C_2H_2O_2^+$ (58.0 amu) and $C_5H_5^+$ (65.0 amu) bands became weaker than those of the 9.5-times cycled electrode, implying less linearity in the polymer structure. The intense signal at 133.0 amu is attributed to the $C_8H_5O_2^+$ fragment with a ring structure, which also supports the possible decrease of linearity in the PET structure. The change in the linearity of the polymer chain could be connected to some modifications in the crystal structure of PET, which in turn affect the diffusivity of lithium ions. A normalized depth profile based on SIMS measurement is also presented in figure 2(f) (see also figures S9 and S10 in the supplementary information). The dominant signals are from lithium ions, and they are distributed close to the PET surface after charge. After discharge, the SIMS intensity of lithiuim ions near the PET surface significantly decreased (figure 2(f)) as the lithium ions were rearranged close to the ITO film (figure S8 in the supplementary information). This result is in good agreement with the visualized PID measurements. XPS measurements were performed to understand the surface chemistry of the electrode including SEI formation upon cycling (figure 3). Some key XPS mappings (214 μm × 214 μm) using core-level energies are presented to confirm that the surface and mass spectrometry analyses are representative, as described in the supplementary information (figures S11–S14). To get a better insight into the formation of the decomposed species from the electrolyte, XPS analyses were also performed on Li 1s, C 1s, O 1s, F 1s and P 2p on both PET and ITO surfaces (figure 3). Figures 3(a)−(d) reveal the XPS analyses on the ITO surface. The Li 1s peak was found at 55.3 eV after electrochemical cycles (last state, charge). The occurrence of these Li^+ fragments can be attributed to the formation of Li_2O during the irreversible conversion reaction and/or Li_2CO_3 and $ROCO_2Li$ (where R represents an organic group) from electrolyte decomposition [78–80]. This result is in accord with the XPS analyses in the region of O 1s. At a deeper location, an extra broad peak could be identified at 56.1 eV. This peak corresponds to the formation of LiF [17, 81]. The spectrum obtained in the C 1s region exhibits two major peaks at 286.3 and 290.0 eV (figure 3(b)), which can be attributed to $ROCO_2Li$ and Li_2CO_3 [80, 82]. This observation is also in good agreement with the XPS analyses of O 1s as well as Li 1s. The chemical properties of C 1s at a deeper

location are similar to those of ITO at the outermost surface. The XPS measurement on F 1s could be fitted with two major peaks at 684.0 eV and 686.0 eV. The peak at 684.0 eV suggests the presence of LiF, while the peak at 686.0 eV indicates the existence of F from $LiPF_6$ (figure 3(c)) [80]. Although our PET as a solid electrolyte is denser than that of a separator application, it is likely to be possible to introduce a small amount of the liquid electrolyte through the film from the PET to ITO direction. As a result, we could observe a F 1s peak (figure 3(c)) attributed to LiF or/and $LiPF_6$. This peak becomes more notable when the XPS spectra are collected at a deeper level below the ITO surface. We have considered this as an indirect contact between the organic electrolyte and the active material through the solid electrolyte, which contributes to retaining a certain level of ionic conductivity between the heteroionic interfaces. In addition, at a deeper level there was a notable change in the peak intensity of LiF and $LiPF_6$. In addition, the peak slightly shifted from 686.0 to 687.0 eV, which implies the formation of $Li_xPO_yF_z$ [80, 83]. As for the P 2p core level, a peak occurred at approximately 134.0 eV after cycling, as presented in figure 3(d), suggesting the formation of $Li_xPO_yF_z$ [80, 84]. This observation is in line with that for the F 1s analysis. It can be deduced from the XPS analyses that the inner part of ITO underwent fewer modifications. On the other hand, some SEI-like species have been found at the gap between ITO and the current collector. Although the observed species are similar to conventional SEI composites, this condition differs from the general SEI case as it is not blocking the diffusion of lithium ions from/into the active material. Contact loss or corrosion of the current collector is obviously another main factor that results in capacity fading and operational failure, but examining this aspect is beyond the scope of the present study. Instead, our further investigation was carried out on the formation of the SEI species on the PET surface, as shown in figures 3(e)−(g). Surprisingly, no decomposed species based on Li, F and P were found in either the pristine (PITO REF) or the cycled state (PITO × 100). This finding is also consistent with the SIMS profile from the PET surface (figure 2(f)). It is thus likely that there was no electrolyte decomposition by PET, and thereby no SEI formation at the PET/electrolyte interface. These results appear to be in line with the SEM analyses, as shown in figure 5(a). The surface morphology of PET hardly changed after the electrochemical cycles. Figure 4 compares the chemical properties of the active material (the ITO side) of the pristine cell (PITO REF) and the cycled cell (PITO × 100). The XPS data with Ar sputtering are also presented to investigate the elemental spectra at a deeper location (figures 4(d)−(f)). The Sn 3d spectrum for the pristine state (PITO REF) exhibits two major peaks with binding energies of 486.2 eV (Sn $3d_{5/2}$) and 494.8 eV (Sn $3d_{3/2}$), as can be seen in figure 4(a). Similarly, there is a doublet in the spectrum of In 3d (figure 4(b)), which can be assigned to In $3d_{5/2}$ (443.3 eV) and In $3d_{3/2}$ (451.9 eV). The spectrum of O 1s can be fitted with two peaks at 529.3 eV and 531.4 eV at the pristine state. The larger peak at 531.4 eV is likely to be ascribed to bulk O^{2-} from In_2O_3, while the smaller peak at 531.0 eV can be attributed to oxygen vacancies in SnO_2 [85–87]. Argon ion sputtering was used to examine the
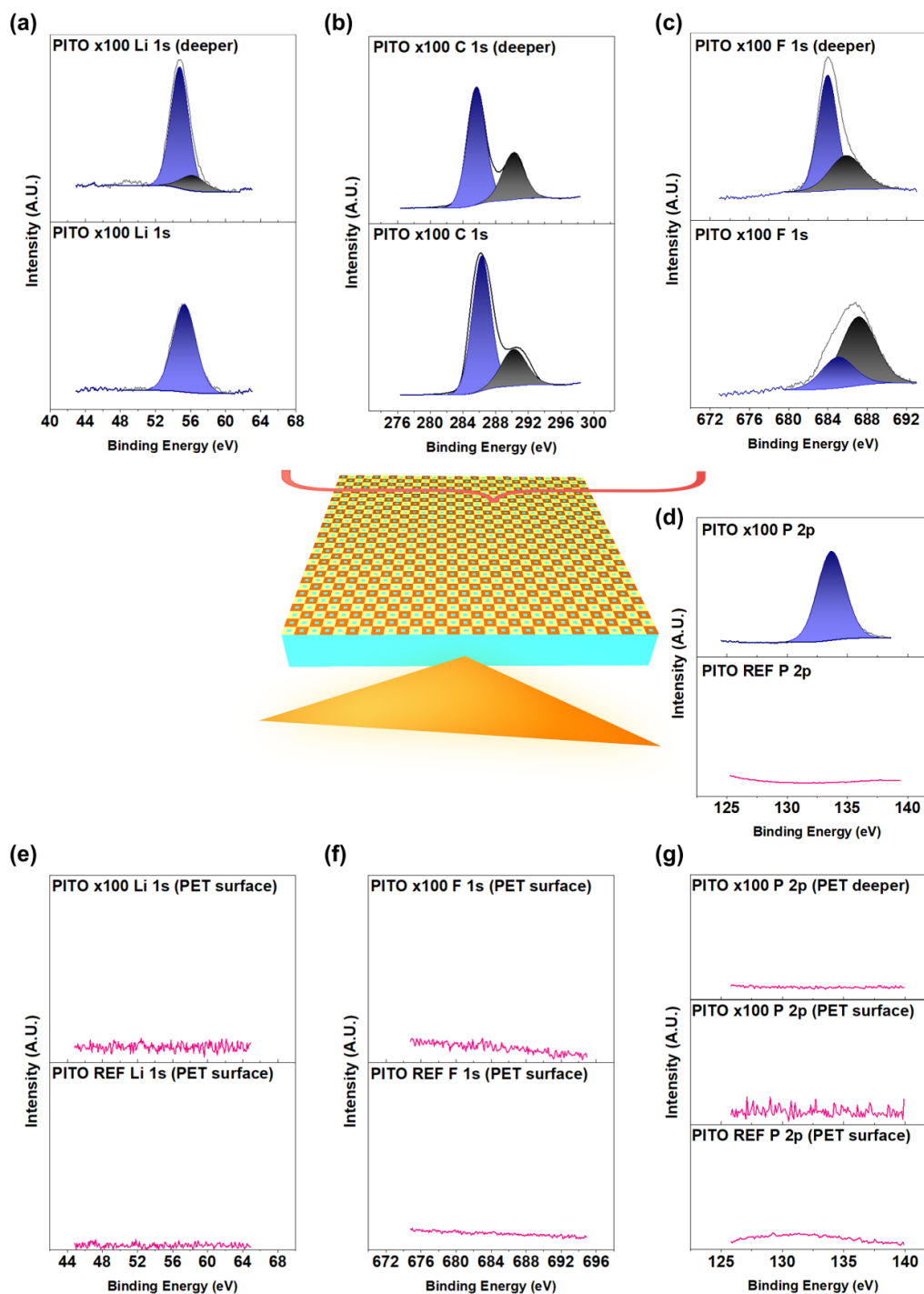
Figure 3. XPS spectra of a PITO 150 nm cell cycled 100 times (PITO × 100) on (a) Li 1s, (b) C 1s, (c) F 1s and (d) P 2p collected from the ITO side, and (e) Li 1s, (f) C 1s and (g) P 2p collected from the PET side.

compositional properties at a deeper location. The spectra of Sn 3d, In 3d and O 1s after the sputtering were almost the same as those of the outer surface measurements, showing good consistency in the composite. Thus, XPS analyses confirmed the successful deposition of ITO on PET. After cycling, there was a notable drop in the peak intensity of In $3d_{5/2}$, In $3d_{3/2}$, Sn $3d_{5/2}$ and Sn $3d_{3/2}$ (figures 4(a) and (b)). This change can be mainly explained by the irreversible conversion of In_2O_3 and SnO_2 into metallic In and Sn, respectively, during the initial

electrochemical cycle. Particular attention has been devoted to the oxidation state changes of the active material. In conventional electrodes, oxidation states of the active material change irreversibly after cycling because of the complex redox reactions between the active material, polymer binder, conductive additive and electrolyte. This oxidation state change can be evaluated from the binding energy shift, and is considered to be a signal of degradation of the battery electrode [12, 88, 89]. Surprisingly, there is little change in the location of those
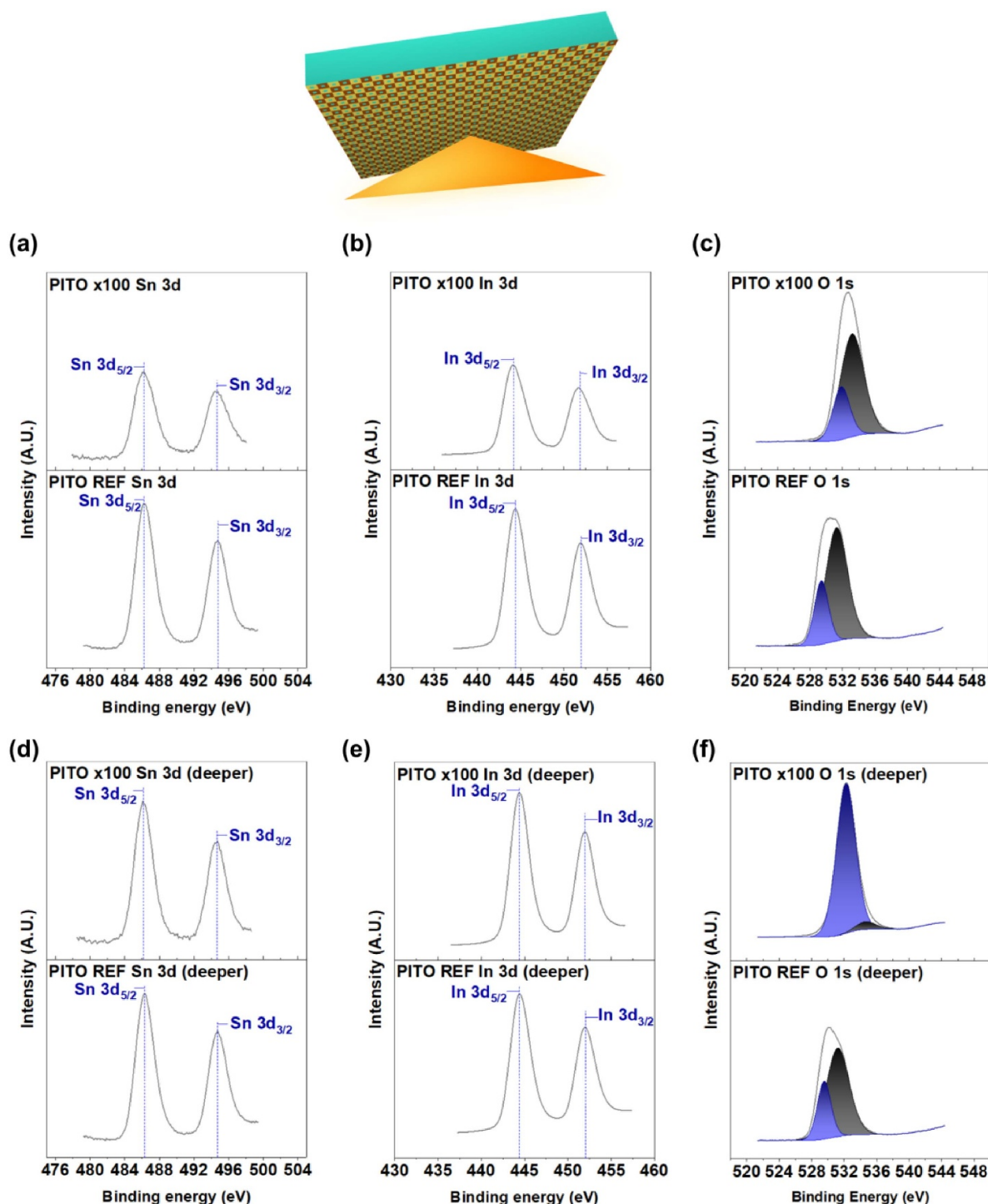
J. Phys. D: Appl. Phys. **54** (2021) 475501

T Kim *et al*

Figure 4. XPS spectra of a PITO 150 nm electrode in the pristine state (PITO REF) and after 100 cycles (PITO × 100) for (a) Sn 3d, (b) In 3d and (c) O 1s at the ITO surface, and (d) Sn 3d, (e) In 3d and (f) O 1s at a greater depth from the ITO surface.

peaks for the PITO, as they remain close to 443.3 eV (In $3d_{5/2}$), 451.9 eV (In $3d_{3/2}$), 486.2 eV (Sn $3d_{5/2}$) and 494.8 eV (Sn $3d_{3/2}$). These doublets correspond to In^{3+} and Sn^{4+}, which are bonded to oxygen atoms of ITO [64, 90, 91]. There has been a certain consumption of the active material as the peak intensity declines upon cycling, but the electrode seems to retain the local atomic environment of the pristine state. As for O 1s, the fitted peaks shifted from 529.3 and 531.4 eV to 531.9 and

533.2 eV, respectively, as shown in figure 4(c). This change indicates some formation of metal carbonates (e.g. Li_2CO_3) and alkyl group species ($ROCO_2Li$) generally resulting from electrolyte decomposition [80, 92, 93]. At a deeper level, those peaks converged into a single large peak at approximately 532.3 eV (figure 4(f)), suggesting the dominant presence of carbonates [78, 80, 92]. On the other hand, interestingly, the spectra of In $3d_{5/2}$, In $3d_{3/2}$, Sn $3d_{5/2}$ and Sn $3d_{3/2}$ of the cycled

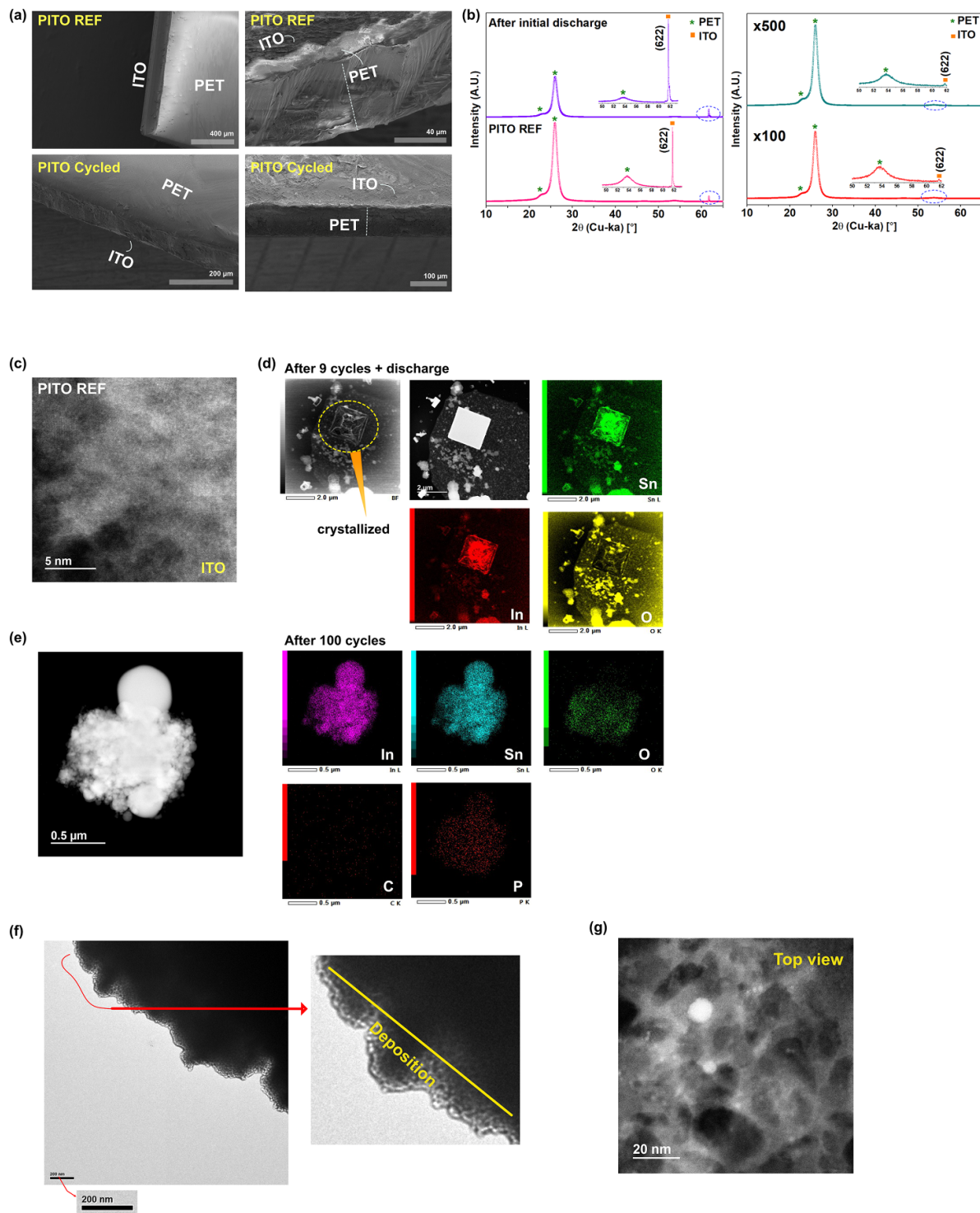J. Phys. D: Appl. Phys. **54** (2021) 475501

T Kim *et al*

Figure 5. (a) SEM comparison of pristine PITO (PITO REF) and PITO after 100 cycles (PITO × 100). (b) XRD powder diffraction results for PET and ITO for pristine PITO (PITO REF), initially discharged, 100-times cycled (PITO × 100) and 500-times cycled (PITO × 500) electrodes. (c) TEM image of pristine PITO, (d) 9.5-cycled PITO and (e) 100-cycled PITO with EDX mapping of Sn L, In L and O K. (f) TEM images of ITO (approximately 150 nm) deposited on PET in the pristine state. (g) Top view of ITO on PET with the presence of voids in the film.

cell at a deeper level were almost the same as those of the pristine state (PITO REF). The intensity did not decrease, nor did a peak shift appear. The outermost surface of ITO lies on top of a current collector, and it is thus the gap between them that allows the formation of some decomposed components stemming from the electrode/electrolyte redox reactions. By contrast, the active material integrated towards PET revealed almost no change in terms of its chemical properties.

As discussed previously, the linearity changes in the polymer (PET) upon cycling are likely to be the key process

involved with lithium ion caging and migration inside the solid electrolyte. A number of fragments that constitute the PET film of cells were identified (figures 2(c)−(e)), and lithium ions seems to be present as $LiCH_3^+$ inside PET. The dimensional modification in the polymer structure appears to be linked to the change in the crystal structure of PET upon cycling (figure 5(b)). In the pristine state (PITO REF) we observe three main crystallography peaks at $2\theta = 22.8°$, $25.9°$ and $53.6°$, which can be assigned to PET [94, 95]. The presence of the broad ($22.8°$) and the sharp ($25.9°$) peaks can be attributed to the semi-crystalline structure of PET [95, 96]. The sharp and large peak at $25.9°$ corresponds to the (100) plane of the PET structure. After the initial discharge, the large peak at $2\theta = 25.9°$ decreased, implying some changes in the crystallinity. This could be the trigger signal of the lithium ion caging process, which would be followed by the increment of linear structures in the polymer. After 100 cycles (PITO × 100), the peak intensity at $25.9°$ increased, recovering almost its initial value. On further cycles up to 500 times (PITO × 500) there was an additional rise in the peak intensity, suggesting better crystallinity in the PET solid electrolyte. It appears that the caged lithium ions could escape due to the improvement in crystallinity of PET upon cycling. This finding also corroborates the observation of improved lithium ion diffusivity upon cycling. The dominant mechanism underlying the crystallization process in PET is likely to be associated with diffusion-induced stress, which is a widely known phenomenon in lithium ion battery electrodes [97, 98]. We believe that the stress induced by lithium ion diffusion exerts a strong influence on crystallization of the PET solid electrolyte at charge–discharge. This effect can be explained by the stress-induced crystallization of PET, which has also been extensively reported [99–101]. By contrast, the crystallographic change of ITO (150 nm) exhibits the opposite trend upon cycling. A small peak was found at approximately $61.6°$, ascribed to the (622) orientation of the cubic structure [102, 103]. After initial charging, the intensity of the (622) peak increased, suggesting the existence of a larger amount of cubic crystalline phase. However, the crystallinity of ITO dramatically decreased on further cycles, as shown in figure 5(b). TEM analyses are also presented in figures 5(c)−(g) (see also figure S16 in the supplementary information). During the early stage of cycling (i.e. 9.5 cycles), we could observe the cubic crystal structure of ITO, as in figure 5(d). While TEM–EDX successfully maps Sn and In, oxygen could be barely detected in the crystal structure. Possibly, this crystallized piece is metallic Sn/In originating from the irreversible conversion reaction during the initial cycle. During the early stage of electrochemical cycles there were several crystallized pieces, but these decrease upon further cycles (PITO × 100). The ITO thin film (PITO 150 nm) became amorphous, as displayed in figure 5(e). This observation is in good agreement with the XRD analyses (figure 5(b)), which reveal the dramatic decline of (622) peaks after 100 and 500 cycles. Some phosphorus was also found by TEM–EDX, suggesting PO bond formation with the electrolyte. Morphological properties of the deposited film can be seen in figures 5(f) and (g). The ITO film with an approximate thickness of 150 nm on the PET substrate

is shown in figure 5(f). From the top view TEM observation (figure 5(g)) we can identify the presence of voids in the film. An attempt has been made to estimate the porosity of the ITO film based on the ratio of the area occupied by the particles (black). There is likely to be 48% void in the deposited film.

4. Conclusions

A hybrid electrolyte comprising a polymeric ionic conductor and a liquid electrolyte has been demonstrated, namely the ITO-PET electrolyte cell (PITO), and revealed high cycling stability at room temperature. Lithium ions are likely to be caged into the PET substrate during electrochemical cycles due to the heteroionic interfaces between the electrolytes with the thin-layer active material (ITO). This configuration leads to the different ion transfer kinetics between charge and discharge. The linear change in the polymer chains and the crystallinity modification are likely to be the key factors for lithium ion migration by $LiCH_3^+$. No decomposed electrolytes or SEI species were identified close to the PET surface, where lithium ion migration takes place. The PITO cells impede the increment in the resistivity of SEI, even in a severely cycled state (PITO × 500), resulting in an excellent rate capability due to the gapless structure of PET/ITO and the simplicity of the electrode composition. We have shown that our PITO cells developed by vacuum sputtering deposition can hinder the formation of electrolyte by-products and SEI species by preventing lithium ions from being trapped in decomposed electrolytes or being turned into SEI species. Taken together, the PITO cell with the hybrid electrolyte has been proved to be useful as an energy storage component for developing stable lithium ion batteries. The present study paves the way to the design of a hybrid electrolyte combining solid and liquid ion conductors for high stability cell operation.

Data availability statement

All data that support the findings of this study are included within the article (and any supplementary files).

ORCID iDs

Taehoon Kim ⓘ https://orcid.org/0000-0003-2145-5293
Luis K Ono ⓘ https://orcid.org/0000-0003-3176-1876
Yabing Qi ⓘ https://orcid.org/0000-0002-4876-8049

References

[1] Tikekar M D, Choudhury S, Tu Z and Archer L A 2016 Design principles for electrolytes and interfaces for stable lithium-metal batteries *Nat. Energy* **1** 16114

[2] Tarascon J-M and Armand M 2001 Issues and challenges facing rechargeable lithium batteries *Nature* **414** 359–67

[3] Lin D, Liu Y and Cui Y 2017 Reviving the lithium metal anode for high-energy batteries *Nat. Nanotechnol.* **12** 194–206

[4] Yamada Y, Furukawa K, Sodeyama K, Kikuchi K, Yaegashi M, Tateyama Y and Yamada A 2014 Unusual stability of acetonitrile-based superconcentrated electrolytes for fast-charging lithium-ion batteries *J. Am. Chem. Soc.* **136** 5039–46

[5] Kim T, Song W, Son D Y, Ono L K and Qi Y B 2019 Lithium-ion batteries: outlook on present, future, and hybridized technologies *J. Mater. Chem.* A **7** 2942–64

[6] Goodenough J B and Kim Y 2010 Challenges for rechargeable Li batteries *Chem. Mater.* **22** 587–603

[7] Goodenough J B and Park K-S 2013 The Li-ion rechargeable battery: a perspective *J. Am. Chem. Soc.* **135** 1167–76

[8] Aurbach D, Zinigrad E, Teller H and Dan P 2000 Factors which limit the cycle life of rechargeable lithium (metal) batteries *J. Electrochem. Soc.* **147** 1274

[9] Lu Y, Tu Z and Archer L A 2014 Stable lithium electrodeposition in liquid and nanoporous solid electrolytes *Nat. Mater.* **13** 961–9

[10] Kim T, Ono L K, Fleck N, Raga S R and Qi Y B 2018 Transition metal speciation as a degradation mechanism with the formation of a solid-electrolyte interphase (SEI) in Ni-rich transition metal oxide cathodes *J. Mater. Chem.* A **6** 14449–63

[11] Kim T, Ono L K and Qi Y B 2019 Elucidating the mechanism involved in the performance improvement of lithium-ion transition metal oxide battery by conducting polymer *Adv. Mater. Interfaces* **6** 1801785

[12] Vetter J, Novák P, Wagner M R, Veit C, K-C M, Besenhard J O, Winter M, Wohlfahrt-Mehrens M, Vogler C and Hammouche A 2005 Ageing mechanisms in lithium-ion batteries *J. Power Sources* **147** 269–81

[13] Joshi T, Eom K, Yushin G and Fuller T F 2014 Effects of dissolved transition metals on the electrochemical performance and SEI growth in lithium-ion batteries *J. Electrochem. Soc.* **161** A1915–21

[14] Cheng X-B B, Zhang R, Zhao C-Z Z, Wei F, Zhang J-G G and Zhang Q 2015 A review of solid electrolyte interphases on lithium metal anode *Adv. Sci.* **3** 1500213

[15] Barré A, Deguilhem B, Grolleau S, Gérard M, Suard F and Riu D 2013 A review on lithium-ion battery ageing mechanisms and estimations for automotive applications *J. Power Sources* **241** 680–9

[16] Arora P, White R E and Doyle M 1998 Capacity fade mechanisms and side reactions in lithium-ion batteries *J. Electrochem. Soc.* **145** 3647

[17] Zhao J *et al* 2017 Surface fluorination of reactive battery anode materials for enhanced stability *J. Am. Chem. Soc.* **139** 11550–8

[18] Lee Y S, Shin W K, Kannan A G, Koo S M and Kim D W 2015 Improvement of the cycling performance and thermal stability of lithium-ion cells by double-layer coating of cathode materials with Al2O3 nanoparticles and conductive polymer *ACS Appl. Mater. Interfaces* **7** 13944–51

[19] Duan H, Yin Y-X, Shi Y, Wang P-F, Zhang X-D, Yang C-P, Shi J-L, Wen R, Guo Y-G and Wan L-J 2018 Dendrite-free Li-metal battery enabled by a thin asymmetric solid electrolyte with engineered layers *J. Am. Chem. Soc.* **140** 82–5

[20] Li Y, Chen X, Dolocan A, Cui Z, Xin S, Xue L, Xu H, Park K and Goodenough J B 2018 Garnet electrolyte with an ultralow interfacial resistance for Li-metal batteries *J. Am. Chem. Soc.* **140** 6448–55

[21] Higgins T M *et al* 2016 A commercial conducting polymer as both binder and conductive additive for silicon nanoparticle-based lithium-ion battery negative electrodes *ACS Nano* **10** 3702–13

[22] Jaber-Ansari L *et al* 2015 Suppressing manganese dissolution from lithium manganese oxide spinel cathodes with single-layer graphene *Adv. Energy Mater.* **5** 1500646

[23] Kim J-S, Kim D W, Jung H T and Choi J W 2015 Controlled lithium dendrite growth by a synergistic effect of multilayered graphene coating and an electrolyte additive *Chem. Mater.* **27** 2780–7

[24] Li J, Dudney N J, Nanda J and Liang C 2014 Artificial solid electrolyte interphase to address the electrochemical degradation of silicon electrodes *ACS Appl. Mater. Interfaces* **6** 10083–8

[25] Zhao J, Lu Z, Wang H, Liu W, Lee H-W, Yan K, Zhuo D, Lin D, Liu N and Cui Y 2015 Artificial solid electrolyte interphase-protected Li$_x$Si nanoparticles: an efficient and stable prelithiation reagent for lithium-ion batteries *J. Am. Chem. Soc.* **137** 8372–5

[26] Fan L, Zhuang H, Gao L, Lu Y and Archer L 2017 Regulating Li deposition at artificial solid electrolyte interphases *J. Mater. Chem.* A **5** 3483–92

[27] Tu Z, Choudhury S, Zachman M J, Wei S, Zhang K, Kourkoutis L F and Archer L A 2018 Fast ion transport at solid–solid interfaces in hybrid battery anodes *Nat. Energy* **3** 310–6

[28] Heine J, Hilbig P, Qi X, Niehoff P, Winter M and Bieker P 2015 Fluoroethylene carbonate as electrolyte additive in tetraethylene glycol dimethyl ether based electrolytes for application in lithium ion and lithium metal batteries *J. Electrochem. Soc.* **162** A1094–101

[29] Kato Y, Hori S, Saito T, Suzuki K, Hirayama M, Mitsui A, Yonemura M, Iba H and Kanno R 2016 High-power all-solid-state batteries using sulfide superionic conductors *Nat. Energy* **1** 16030

[30] Pervez S A, Cambaz M A, Thangadurai V and Fichtner M 2019 Interface in solid-state lithium battery: challenges, progress, and outlook *ACS Appl. Mater. Interfaces* **11** 22029–50

[31] Yu C, Ganapathy S, Van Eck E R H, Wang H, Basak S, Li Z and Wagemaker M 2017 Accessing the bottleneck in all-solid state batteries, lithium-ion transport over the solid-electrolyte-electrode interface *Nat. Commun.* **8** 1086

[32] Liu H *et al* 2020 Controlling dendrite growth in solid-state electrolytes *ACS Energy Lett.* **5** 833–43

[33] Santhanagopalan D, Qian D, McGilvray T, Wang Z, Wang F, Camino F, Graetz J, Dudney N and Meng Y S 2014 Interface limited lithium transport in solid-state batteries *J. Phys. Chem. Lett.* **5** 298–303

[34] Wang Z, Santhanagopalan D, Zhang W, Wang F, Xin H L, He K, Li J, Dudney N and Meng Y S 2016 *In situ* STEM-EELS observation of nanoscale interfacial phenomena in all-solid-state batteries *Nano Lett.* **16** 3760–7

[35] Jiang C, Li H and Wang C 2017 Recent progress in solid-state electrolytes for alkali-ion batteries *Sci. Bull.* **62** 1473–90

[36] Sun C, Liu J, Gong Y, Wilkinson D P and Zhang J 2017 Recent advances in all-solid-state rechargeable lithium batteries *Nano Energy* **33** 363–86

[37] Chen R, Qu W, Guo X, Li L and Wu F 2016 The pursuit of solid-state electrolytes for lithium batteries: from

J. Phys. D: Appl. Phys. **54** (2021) 475501

T Kim *et al*

comprehensive insight to emerging horizons *Mater. Horizons* **3** 487–516

[38] Dawson J A, Naylor A J, Eames C, Roberts M, Zhang W, Snaith H J, Bruce P G and Islam M S 2017 Mechanisms of lithium intercalation and conversion processes in organic–inorganic halide perovskites *ACS Energy Lett.* **2** 1818–24

[39] Bachman J C *et al* 2016 Inorganic solid-state electrolytes for lithium batteries: mechanisms and properties governing ion conduction *Chem. Rev.* **116** 140–62

[40] Song S, Kotobuki M, Zheng F, Xu C, Savilov S V, Hu N, Lu L, Wang Y and Li W D Z 2017 A hybrid polymer/oxide/ionic-liquid solid electrolyte for Na-metal batteries *J. Mater. Chem.* A **5** 6424–31

[41] Tang J, Wang L, You L, Chen X, Huang T, Zhou L, Geng Z and Yu A 2021 Effect of organic electrolyte on the performance of solid electrolyte for solid–liquid hybrid lithium batteries *ACS Appl. Mater. Interfaces* **13** 2685−93

[42] Kim H W, Manikandan P, Lim Y J, Kim J H, Nam S C and Kim Y 2016 Hybrid solid electrolyte with the combination of Li$_7$La$_3$Zr$_2$O$_{12}$ ceramic and ionic liquid for high voltage pseudo-solid-state Li-ion batteries *J. Mater. Chem.* A **4** 17025–32

[43] Busche M R, Drossel T, Leichtweiss T, Weber D A, Falk M, Schneider M, Reich M L, Sommer H, Adelhelm P and Janek J 2016 Dynamic formation of a solid-liquid electrolyte interphase and its consequences for hybrid-battery concepts *Nat. Chem.* **8** 426–34

[44] Weiss M, Simon F J, Busche M R, Nakamura T, Schröder D, Richter F H and Janek J 2020 From liquid- to solid-state batteries: ion transfer kinetics of heteroionic interfaces *Electrochem. Energy Rev.* **3** 221–38

[45] Lewis B G and Paine D C 2000 Applications and processing of transparent conducting oxides *MRS Bull.* **25** 22–27

[46] Lee J, Jung H, Lee J, Lim D, Yang K, Yi J and Song W-C 2008 Growth and characterization of indium tin oxide thin films deposited on PET substrates *Thin Solid Films* **516** 1634–9

[47] Cheng Y-T, Ho J-J, Wang C-K, Lee W, Lu C-C, Yau B-S, Nain J-L, Chang S-H, Chang C-C and Wang K L 2010 Improvement of organic solar cells by flexible substrate and ITO surface treatments *Appl. Surf. Sci.* **256** 7606–11

[48] Jeong H-S, Kim J H and Lee S-Y 2010 A novel poly(vinylidene fluoride-hexafluoropropylene)/poly(ethylene terephthalate) composite nonwoven separator with phase inversion-controlled microporous structure for a lithium-ion battery *J. Mater. Chem.* **20** 9180

[49] Cai H, Tong X, Chen K, Shen Y, Wu J, Xiang Y, Wang Z and Li J 2018 Electrospun polyethylene terephthalate nonwoven reinforced polypropylene separator: scalable synthesis and its lithium ion battery performance *Polymers* **10** 574

[50] Zhang W, Nie J, Li F, Wang Z L and Sun C 2018 A durable and safe solid-state lithium battery with a hybrid electrolyte membrane *Nano Energy* **45** 413–9

[51] Zhu C, Nagaishi T, Shi J, Lee H, Wong P Y, Sui J, Hyodo K and Kim I S 2017 Enhanced wettability and thermal stability of a novel polyethylene terephthalate-based poly(vinylidene fluoride) nanofiber hybrid membrane for the separator of lithium-ion batteries *ACS Appl. Mater. Interfaces* **9** 26400–6

[52] Lee J-R, Won J-H, Kim J H, Kim K J and Lee S-Y 2012 Evaporation-induced self-assembled silica colloidal particle-assisted nanoporous structural evolution of poly(ethylene terephthalate) nonwoven composite separators for high-safety/high-rate lithium-ion batteries *J. Power Sources* **216** 42–7

[53] Hao J, Lei G, Li Z, Wu L, Xiao Q and Wang L 2013 A novel polyethylene terephthalate nonwoven separator based on electrospinning technique for lithium ion battery *J. Memb. Sci.* **428** 11–6

[54] Freire M T D A, Damant A P, Castle L and Reyes F G R 1999 Thermal stability of polyethylene terephthalate (PET): oligomer distribution and formation of volatiles *Packag. Technol. Sci.* **12** 29–36

[55] Sun P, Lu H, Zhang W, Wu H, Sun S and Liu X 2018 Poly(ethylene terephthalate): rubbish could be low cost anode material of lithium ion battery *Solid State Ion.* **317** 164–9

[56] Pandey M, Manoj B, Joshi G M, Ghosh N N and Vendan A S 2019 Superior charge discharge ability of reduced graphene oxide/Li-ion embedded polymer composite films *J. Mater. Sci. Mater. Electron.* **30** 2136–45

[57] Pandey M, Joshi G M and Ghosh N N 2016 Electrical performance of lithium ion based polymer electrolyte with polyethylene glycol and polyvinyl alcohol network *Int. J. Polym. Mater. Polym. Biomater.* **65** 759–68

[58] Courtney I A and Dahn J R 1997 Electrochemical and *in situ* x-ray diffraction studies of the reaction of lithium with tin oxide composites *J. Electrochem. Soc.* **144** 2045

[59] Liu X, Zhang J, Si W, Xi L, Oswald S, Yan C and Schmidt O G 2015 High-rate amorphous SnO$_2$ nanomembrane anodes for Li-ion batteries with a long cycling life *Nanoscale* **7** 282–8

[60] Kim H *et al* 2014 New insight into the reaction mechanism for exceptional capacity of ordered mesoporous SnO$_2$ electrodes via synchrotron-based x-ray analysis *Chem. Mater.* **26** 6361–70

[61] Winter M and Besenhard J O 1999 Electrochemical lithiation of tin and tin-based intermetallics and composites *Electrochim. Acta* **45** 31–50

[62] Larcher D, Beattie S, Morcrette M, Edström K, Jumas J-C and Tarascon J-M 2007 Recent findings and prospects in the field of pure metals as negative electrodes for Li-ion batteries *J. Mater. Chem.* **17** 3759

[63] Chen J S and Lou X W D 2013 SnO$_2$-based nanomaterials: synthesis and application in lithium-ion batteries *Small* **9** 1877–93

[64] Yang H, Song T, Lee S, Han H, Xia F, Devadoss A, Sigmund W and Paik U 2013 Tin indium oxide/graphene nanosheet nanocomposite as an anode material for lithium ion batteries with enhanced lithium storage capacity and rate capability *Electrochim. Acta* **91** 275–81

[65] Kalubarme R S, Lee J-Y and Park C-J 2015 Carbon encapsulated tin oxide nanocomposites: an efficient anode for high performance sodium-ion batteries *ACS Appl. Mater. Interfaces* **7** 17226–37

[66] Abouali S, Akbari Garakani M and Kim J-K 2018 Ultrafine SnO$_2$ nanoparticles encapsulated in ordered mesoporous carbon framework for Li-ion battery anodes *Electrochim. Acta* **284** 436–43

[67] Heubner C, Liebmann T, Voigt K, Weiser M, Matthey B, Junker N, Lämmel C, Schneider M and Michaelis A 2018 Scalable fabrication of nanostructured tin oxide anodes for high-energy lithium-ion batteries *ACS Appl. Mater. Interfaces* **10** 27019–29

[68] Kaskhedikar N A and Maier J 2009 Lithium storage in carbon nanostructures *Adv. Mater.* **21** 2664–80

[69] Persson K, Hinuma Y, Meng Y S, Van Der Ven A and Ceder G 2010 Thermodynamic and kinetic properties of the Li-graphite system from first-principles calculations *Phys. Rev.* B **82** 125416

[70] Xu C, Lindgren F, Philippe B, Gorgoi M, Björefors F, Edström K and Gustafsson T 2015 Improved performance of the silicon anode for li-ion batteries: understanding the surface modification mechanism of fluoroethylene carbonate as an effective electrolyte additive *Chem. Mater.* **27** 2591–9

J. Phys. D: Appl. Phys. **54** (2021) 475501

T Kim *et al*

[71] Yuca N and Ü Ç 2016 A facile and functional process to enhance electrochemical performance of silicon anode in lithium ion batteries *Electrochim. Acta* **222** 1538–44

[72] Shang Y, Lin X, Lu X, Huang T and Yu A 2015 Nano-TiO$_2$(B) coated LiMn$_2$O$_4$ as cathode materials for lithium-ion batteries at elevated temperatures *Electrochim. Acta* **156** 121–6

[73] Oh G, Hirayama M, Kwon O, Suzuki K and Kanno R 2016 Bulk-type all solid-state batteries with 5 V class LiNi$_{0.5}$Mn$_{1.5}$ O$_4$ cathode and Li$_{10}$GeP$_2$S$_{12}$ solid electrolyte *Chem. Mater.* **28** 2634–40

[74] Gnanaraj J S, Thompson R W, Iaconatti S N, DiCarlo J F and Abraham K M 2005 Formation and growth of surface films on graphitic anode materials for Li-ion batteries *Electrochem. Solid-State Lett.* **8** A128

[75] Jaumann T *et al* 2017 Lifetime vs. rate capability: understanding the role of FEC and VC in high-energy Li-ion batteries with nano-silicon anodes *Energy Storage Mater.* **6** 26–35

[76] Lee J and Choi W 2015 Surface modification of over-lithiated layered oxides with PEDOT:PSS conducting polymer in lithium-ion batteries *J. Electrochem. Soc.* **162** A743–8

[77] Endo K, Hayashi K, Ida T, Matsumoto D and Kato N 2010 Theoretical mass spectra of PE, PP, PS and PET polymers by QMD methods using the model molecules *J. Surf. Anal.* **17** 2–14

[78] Eriksson T, Andersson A M, Bishop A G, Gejke C, Gustafsson T and Thomas J O 2002 Surface analysis of LiMn$_2$O$_4$ electrodes in carbonate-based electrolytes *J. Electrochem. Soc.* **149** A69

[79] Wang X *et al* 2017 New insights on the structure of electrochemically deposited lithium metal and its solid electrolyte interphases via cryogenic TEM *Nano Lett.* **17** 7606–12

[80] Andersson A M, Abraham D P, Haasch R, MacLaren S, Liu J and Amine K 2002 Surface characterization of electrodes from high power lithium-ion batteries *J. Electrochem. Soc.* **149** A1358

[81] Chattopadhyay S, Lipson A L, Karmel H J, Emery J D, Fister T T, Fenter P A, Hersam M C and Bedzyk M J 2012 *In situ* x-ray study of the solid electrolyte interphase (SEI) formation on graphene as a model Li-ion battery anode *Chem. Mater.* **24** 3038–43

[82] Yen Y-C, Chao S-C, Wu H-C and Wu N-L 2009 Study on solid-electrolyte-interphase of Si and C-coated Si electrodes in lithium cells *J. Electrochem. Soc.* **156** A95

[83] Eriksson T, Andersson A M, Gejke C, Gustafsson T and Thomas J O 2002 Influence of temperature on the interface chemistry of Li$_x$Mn$_2$O$_4$ electrodes *Langmuir* **18** 3609–19

[84] Duncan H, Duguay D, Abu-Lebdeh Y and Davidson I J 2011 Study of the LiMn$_{1.5}$Ni$_{0.5}$O$_4$/electrolyte interface at room temperature and 60 °C *J. Electrochem. Soc.* **158** A537

[85] Peng X S, Meng G W, Wang X F, Wang Y W, Zhang J, Liu X and Zhang L D 2002 Synthesis of oxygen-deficient indium-tin-oxide (ITO) nanofibers *Chem. Mater.* **14** 4490–3

[86] Alam M and Cameron D 2002 Investigation of annealing effects on sol–gel deposited indium tin oxide thin films in different atmospheres *Thin Solid Films* **420–421** 76–82

[87] Misra M, Hwang D-K, Kim Y C, Myoung J-M and Il L T 2018 Eco-friendly method of fabricating indium-tin-oxide thin films using pure aqueous sol-gel *Ceram. Int.* **44** 2927–33

[88] Radin M D, Hy S, Sina M, Fang C, Liu H, Vinckeviciute J, Zhang M, Whittingham M S, Meng Y S and Van Der Ven A 2017 Narrowing the gap between theoretical and practical capacities in Li-ion layered oxide cathode materials *Adv. Energy Mater.* **7** 1602888

[89] Choi N-S, Han J-G, Ha S-Y, Park I and Back C-K 2015 Recent advances in the electrolytes for interfacial stability of high-voltage cathodes in lithium-ion batteries *RSC Adv.* **5** 2732–48

[90] Teixeira V, Cui H, Meng L, Fortunato E and Martins R 2002 Amorphous ITO thin films prepared by DC sputtering for electrochromic applications *Thin Solid Films* **420–421** 70–75

[91] Khan G G, Ghosh S, Sarkar A, Mandal G, Mukherjee G D, Manju U, Banu N and Dev B N 2015 Defect engineered *d*^{0} ferromagnetism in tin-doped indium oxide nanostructures and nanocrystalline thin-films *J. Appl. Phys.* **118** 074303

[92] Cherkashinin G, Nikolowski K, Ehrenberg H, Jacke S, Dimesso L and Jaegermann W 2012 The stability of the SEI layer, surface composition and the oxidation state of transition metals at the electrolyte–cathode interface impacted by the electrochemical cycling: x-ray photoelectron spectroscopy investigation *Phys. Chem. Chem. Phys.* **14** 12321

[93] Gauthier M *et al* 2015 Electrode–electrolyte interface in Li-ion batteries: current understanding and new insights *J. Phys. Chem. Lett.* **6** 4653–72

[94] Kuwabara T, Wang X, Kusumi T, Yamaguchi T, Taima T and Takahashi K 2016 Flexible inverted polymer solar cells fabricated in air at low temperatures *Japan. J. Appl. Phys.* **55** 086501

[95] Mallick B 2015 X-ray diffraction analysis of polymeric solid using Bragg-Brentano geometry *Int. J. Mat. Chem. Phys.* **1** 265–70

[96] Martins C R, De Almeida Y M, Do Nascimento G C and De Azevedo W M 2006 Metal nanoparticles incorporation during the photopolymerization of polypyrrole *J. Mater. Sci.* **41** 7413–8

[97] Tavassol H, Jones E M C, Sottos N R and Gewirth A A 2016 Electrochemical stiffness in lithium-ion batteries *Nat. Mater.* **15** 1182–7

[98] Chon M J, Sethuraman V A, McCormick A, Srinivasan V and Guduru P R 2011 Real-time measurement of stress and damage evolution during initial lithiation of crystalline silicon *Phys. Rev. Lett.* **107** 045503

[99] Misra A and Stein R S 1979 Stress-induced crystallization of poly(ethylene terephthalate) *J. Polym. Sci. Polym. Phys. Ed.* **17** 235–57

[100] Jabarin S A 1992 Strain-induced crystallization of poly(ethylene terephthalate) *Polym. Eng. Sci.* **32** 1341–9

[101] Mascia L and Fekkai Z 1993 Influence of stress-induced crystallization on the dimensional stability of monoaxially drawn poly(ethylene terephthalate) *Polymer* **34** 1418–22

[102] Son P, Choi S-W and Kim S 2012 Indium tin oxide exhibiting high poly-crystallinity on oxygen plasma-treated polyethylene terephthalate surface *Nanoscale Res. Lett.* **7** 118

[103] Choi D, Hong S-J and Son Y 2014 Characteristics of indium tin oxide (ITO) nanoparticles recovered by lift-off method from TFT-LCD panel scraps *Materials* **7** 7662–9